1 **Impacts of aerosol-photolysis interaction and aerosol-radiation**

2 **feedback on surface-layer ozone in North China during multi-**

3 **pollutant air pollution episodes**

4

5 Hao Yang[1], Lei Chen[1], Hong Liao[1], Jia Zhu[1], Wenjie Wang[2], Xin Li[2]

6

7 [1]Jiangsu Key Laboratory of Atmospheric Environment Monitoring and Pollution

8 Control, Jiangsu Collaborative Innovation Center of Atmospheric Environment and

9 Equipment Technology, School of Environmental Science and Engineering, Nanjing

10 University of Information Science & Technology, Nanjing 210044, China

11 [2]State Joint Key Laboratory of Environmental Simulation and Pollution Control,

12 College of Environmental Sciences and Engineering, Peking University, Beijing

13 100871, China

14

15 **Correspondence:** Lei Chen (chenlei@nuist.edu.cn) and Hong Liao

16 (hongliao@nuist.edu.cn)

17

Abstract

We examined the impacts of aerosol-radiation interactions, including the effects of aerosol-photolysis interaction (API) and aerosol-radiation feedback (ARF), on surface-layer ozone (O_3) concentrations during three multi-pollutant air pollution episodes characterized by high O_3 and $PM_{2.5}$ levels during 28 July to 3 August 2014 (Episode1), 8-13 July 2015 (Episode2) and 5-11 June 2016 (Episode3) in North China, by using the Weather Research and Forecasting with Chemistry (WRF-Chem) model embedded with an integrated process analysis scheme. Our results show that aerosol-radiation interactions decreased the daytime shortwave radiation at surface by $92.4 \sim 100.3$ W m^{-2} averaged over the complex air pollution areas in these three episodes. The dimming effect reduced the near-surface photolysis rates of J[NO_2] and J[O^1D] by $1.8 \times 10^{-3} \sim 2.0 \times 10^{-3}$ s^{-1} and $5.7 \times 10^{-6} \sim 6.3 \times 10^{-6}$ s^{-1}, respectively. However, the daytime shortwave radiation in the atmosphere was increased by $72.8 \sim 85.2$ W m^{-2}, which made the atmosphere more stable. The stabilized atmosphere decreased the planetary boundary layer height and 10 m wind speed by $129.0 \sim 249.0$ m and $0.05 \sim 0.12$ m s^{-1}, respectively. The weakened photolysis rates and changed meteorological conditions reduced daytime surface-layer O_3 concentrations by up to $9.3 \sim 11.4$ ppb, with API and ARF contributing $74.6\% \sim 90.0\%$ and $10.0\% \sim 25.4\%$ of the O_3 decrease in these three episodes, respectively. Process analysis indicated that the weakened O_3 chemical production made the greatest contribution to API effect while the reduced vertical mixing was the key process for ARF effect. This study implies that future $PM_{2.5}$ reductions will lead to O_3 increases due to weakened aerosol-radiation interactions. Therefore, tighter controls of O_3 precursors are needed to offset O_3 increases caused by weakened aerosol-radiation interactions in the future.

1 Introduction

China has been experiencing severe air pollution in recent years, characterized by high loads of $PM_{2.5}$ (particulate matter with an aerodynamic equivalent diameter of 2.5 micrometers or less) and high levels of ozone (O_3). Observational studies exhibited positive correlations and synchronous occurrence of $PM_{2.5}$ and O_3 pollution in North China during summer (Zhao et al., 2018; Zhu et al., 2019), indicating that complex air pollution is becoming a major challenge for North China.

Aerosols can absorb and scatter solar radiation to affect Earth's energy balance. They can also act as cloud condensation nuclei and ice nuclei, and further modify the microphysical characteristics of clouds (Albrecht et al., 1989; Haywood et al., 2000; Lohmann et al., 2005). Both ways perturb meteorological variables, e.g., temperature, planetary boundary layer height (PBLH), and precipitation, and eventually influence air pollutants (Petäjä et al., 2016; Miao et al., 2018; Zhang et al., 2018). Many studies are focused on the feedback between aerosol and meteorology (Gao et al., 2015; Gao et al., 2016a; Qiu et al., 2017; Chen et al., 2019; Zhu et al., 2021). Gao et al. (2015) used the WRF-Chem model to investigate the feedbacks between aerosols and meteorological variables over the North China Plain in January 2013, and pointed out that aerosols could cause a decrease in surface temperature by 0.8-2.8 °C but an increase of 0.1-0.5 °C around 925 hPa. The more stable atmosphere caused by surface cooling and higher layer heating led to the decreases of surface wind speed and PBLH by 0.3 m s^{-1} and 40-200 m, respectively, which further resulted in overall $PM_{2.5}$ increases by 10-50 μg m^{-3} (2-30%). By using the same WRF-Chem model, Qiu et al. (2017) reported that the surface downward shortwave radiation and PBLH were reduced by 54.6 W m^{-2} and 111.4 m due to aerosol radiative forcing during 21 and 27 February 2014 in the North China Plain. As a result, the surface $PM_{2.5}$ concentration averaged over the North China Plain was increased by 34.9 μg m^{-3} (20.4%).

Aerosols can also influence O_3 through aerosol-radiation interactions, including aerosol-photolysis interaction and aerosol-radiation feedback. Aerosols can scatter and absorb UV radiation, and therefore directly affect O_3 photochemistry reactions,

71 which is called aerosol-photolysis interaction (API) (Dickerson et al., 1997; Liao et al.,

72 1999; Li et al., 2011; Lou et al., 2014). The changed meteorological variables due to

73 aerosol radiative forcing can indirectly affect O_3 concentrations, which is called

74 aerosol-radiation feedback (ARF) (Hansen et al., 1997; Gao et al., 2018; Liu et al.,

75 2020). Although the effects of API or ARF on O_3 have been examined by previous

76 studies (Xing et al., 2017; Gao et al., 2018; Gao et al., 2020), the combined effects of

77 API and ARF on O_3, especially under the conditions of synchronous occurrence of

78 high $PM_{2.5}$ and O_3 concentrations, remain largely elusive.

79   The present study aims to (1) quantify the respective/combined contributions of

80 API and ARF on surface O_3 concentrations by using the WRF-Chem model; (2)

81 explore the prominent physical and/or chemical processes responsible for API and

82 ARF effects by using an integrated process rate (IPR) analysis embedded in WRF-

83 Chem model. In order to draw the general conclusions, three multi-pollutant air

84 pollution episodes characterized by high O_3 and $PM_{2.5}$ levels during 28 July to 3

85 August 2014 (Episode1), 8-13 July 2015 (Episode2) and 5-11 June 2016 (Episode3)

86 in North China are analyzed in this study. The model configuration, numerical

87 experiments, observational data, and the integrated process rate analysis are described

88 in section 2. Section 3 shows the model evaluation. The presentation and discussion

89 of the model results are exhibited in section 4, and the conclusions and discussions are

90 provided in section 5.

91 **2 Methods**

92 **2.1 Model configuration**

93   The version 3.7.1 of the online-coupled Weather Research and Forecasting with

94 Chemistry (WRF-Chem) model (Grell et al., 2005; Skamarock et al., 2008) is used in

95 this study to explore the impacts of aerosol-radiation interactions on surface-layer O_3

96 in North China. WRF-Chem can simulate gas phase species and aerosols coupled with

97 meteorological fields, and has been widely used to investigate air pollution over North

98 China (Gao et al., 2016a; Gao et al., 2020; Wu et al., 2020). As shown in Fig. 1, we

99 design two nested model domains with the number of grid points of 57 (west–east) ×

100 41 (south–north) and 37 (west–east) × 43 (south–north) at 27 and 9 km horizontal

101 resolutions, respectively. The parent domain centers at (39 °N, 117 °E). The model

102 contains 29 vertical levels from the surface to 50 hPa, with 14 levels below 2 km for

103 the fully description of the vertical structure of planetary boundary layer (PBL).

104 　　The Carbon Bond Mechanism Z (CBM-Z) is selected as the gas-phase chemical

105 mechanism (Zaveri and Peters, 1999), and the full 8-bin MOSAIC (Model for

106 Simulating Aerosol Interactions and Chemistry) aerosol module with aqueous

107 chemistry is used to simulate aerosol evolution (Zaveri et al., 2008). The photolysis

108 rates are calculated by the Fast-J scheme (Wild et al., 2000). Other major physical

109 parameterizations used in this study are listed in Table 1.

110 　　The initial and boundary meteorological conditions are provided by the National

111 Centers for Environmental Prediction (NCEP) Final Analysis data with a spatial

112 resolution of $1° \times 1°$. In order to limit the model bias of simulated meteorological

113 fields, the four-dimensional data assimilation (FDDA) is used with the nudging

114 coefficient of 3.0×10^{-4} for wind, temperature and humidity (no analysis nudging is

115 applied for the inner domain) (Lo et al., 2008; Otte, 2008). Chemical initial and

116 boundary conditions are obtained from the Model for Ozone and Related chemical

117 Tracers, version 4 (MOZART-4) forecasts (Emmons et al., 2010).

118 　　Anthropogenic emissions in Episode1 are taken from the 2010 MIX Asian

119 emission inventory, and the Multi-resolution Emission Inventory for China (MEIC) is

120 used in Episode2 and Episode3 (http://www.meicmodel.org/) (Li et al., 2017a). These

121 emission inventories provide emissions of sulfur dioxide (SO_2), nitrogen oxides (NO_x),

122 carbon monoxide (CO), non-methane volatile organic compounds (NMVOCs), carbon

123 dioxide (CO_2), ammonia (NH_3), black carbon (BC), organic carbon (OC), PM_{10}

124 (particulate matter with aerodynamic diameter is 10 µm and less) and $PM_{2.5}$.

125 Emissions are aggregated from four sectors, including power generation, industry,

126 residential, and transportation, with $0.25° \times 0.25°$ spatial resolution. Biogenic

127 emissions are calculated online by the Model of Emissions of Gases and Aerosols

128 from Nature (MEGAN) (Guenther et al., 2006).

2.2 Numerical experiments

To quantify the impacts of API and ARF on O_3, three case simulations have been conducted: (1) BASE – the base simulation coupled with the interactions between aerosol and radiation, which includes both impacts of API and ARF; (2) NOAPI – the same as the BASE case, but the impact of API is turned off (aerosol optical properties are set to zero in the photolysis module), following Wu et al. (2020); (3) NOALL – both the impacts of API and ARF are turned off (removing the mass of aerosol species when calculating aerosol optical properties in the optical module), following Qiu et al. (2017). The differences between BASE and NOAPI (i.e., BASE minus NOAPI) represent the impacts of API. The contributions from ARF can be obtained by comparing NOAPI and NOALL (i.e., NOAPI minus NOALL). The combined effects of API and ARF on O_3 concentrations can be quantitatively evaluated by the differences between BASE and NOALL (i.e., BASE minus NOALL).

All the experiments in Episode1, Episode2 and Episode3 are conducted from 26 July to 3 August 2014, 6-13 July 2015 and 3-11 June 2016, respectively, with the first 40 hours as the model spin-up in each case. Simulation results from the BASE cases of the three episodes are used to evaluate the model performance.

2.3 Observational data

Simulation results are compared with meteorological and chemical measurements. The surface-layer meteorological data (2 m temperature (T_2), 2 m relative humidity (RH_2), and 10 m wind speed (WS_{10})) with the temporal resolution of 3 h at ten stations (Table S1) are obtained from NOAA's National Climatic Data Center (https://gis.ncdc.noaa.gov/maps/ncei/cdo/hourly). The radiosonde data of temperature at 08:00 and 20:00 LST in Beijing (39.93 °N, 116.28 °E) are provided by the University of Wyoming (http://weather.uwyo.edu/). Observed hourly concentrations of $PM_{2.5}$ and O_3 at thirty-two sites (Table S2) in North China are collected from the China National Environmental Monitoring Center (CNEMC). The photolysis rate of nitrogen dioxide ($J[NO_2]$) measured at the Peking University site (39.99 °N, 116.31 °E) is also used to evaluate the model performance. More details

158 about the measurement technique of J[NO$_2$] can be found in Wang et al. (2019). The

159 aerosol optical depth (AOD) at Beijing site (39.98°N, 116.38°E) is provided by

160 AERONET (level 2.0, http://aeronet.gsfc.nasa.gov/). The AOD at 675 nm and 440 nm

161 are used to derive the AOD at 550 nm to compare with the simulated ones.

162 **2.4 Integrated process rate analysis**

163 Integrated process rate (IPR) analysis has been widely used to quantify the

164 contributions of different processes to O$_3$ variations (Goncalves et al., 2009; Gao et al.,

165 2016b; Tang et al., 2017; Gao et al., 2018). In this study, four physical/chemical

166 processes are considered, including vertical mixing (VMIX), net chemical production

167 (CHEM), horizontal advection (ADVH), and vertical advection (ADVZ). VMIX is

168 initiated by turbulent process and closely related to PBL development, which

169 influences O$_3$ vertical gradients. CHEM represents the net O$_3$ chemical production

170 (chemical production minus chemical consumption). ADVH and ADVZ represent

171 transport by winds (Gao et al., 2016b). In this study, we define ADV as the sum of

172 ADVH and ADVZ.

3 Model evaluation

173

174 Reasonable representation of observed meteorological and chemical variables by

175 the WRF-Chem model can provide foundation for evaluating the impacts of aerosols

176 on surface-layer ozone concentrations. The model results presented in this section are

177 taken from the BASE cases in the three episodes. The concentrations of air pollutants

178 are averaged over the thirty-two observation sites in Beijing, Tianjin and Baoding. To

179 ensure the data quality, the mean value for each time is calculated only when

180 concentrations are available at more than sixteen sites, as did in Li et al. (2019a).

3.1 Chemical simulations

181

182 Figure 2 shows the temporal variations of observed and simulated PM$_{2.5}$ and O$_3$

183 concentrations over North China for the three episodes. As shown in Fig. 2, the

184 temporal variations of observed PM$_{2.5}$ can be well performed by the model with

185 correlation coefficients (R) of 0.66, 0.56 and 0.73 and normalized mean bias (NMB)

186   of -19.2%, -3.9% and 30.4% during Episode1, Episode2 and Episode3, respectively.

187   The model also tracks well the diurnal variation of O_3 over the North China, with R of

188   0.86, 0.91 and 0.86 and NMB of -12.0%, 0.4% and 1.6% for Episode1, Episode2 and

189   Episode3, respectively.

190   Figure S1 shows the correlation between observed and simulated AOD at 550

191   nm in Beijing. In the WRF-Chem model, the AOD at 550 nm are calculated by using

192   the values at 400 and 600 nm according to the Angstrom exponent. Analyzing Fig. S1,

193   the model can reproduce the observed AOD with R of 0.7 and NMB of 7.9%.

194   **3.2 Meteorological simulations**

195   Figure 3 shows the time series of observed and simulated T_2, RH_2, WS_{10} and

196   $J[NO_2]$ during the three episodes. The observed T_2, RH_2, WS_{10} are averaged over the

197   ten meteorological observation stations, and the $J[NO_2]$ are measured at Peking

198   University. Most of the monitored $J[NO_2]$ in Episode3 are unavailable, so the

199   comparison of $J[NO_2]$ in Episode3 is not shown. Generally, the model can depict the

200   temporal variations of T_2 fairly well with R of 0.98 and the mean bias (MB) of -1.9~-

201   0.9 °C. For RH_2, the R and MB are 0.91~0.97 and -4.0%~1.9%, respectively.

202   Although WRF-Chem model overestimates WS_{10} with the MB of 0.6~0.9 m s^{-1}, the R

203   for WS_{10} is 0.70~0.89 and the root-mean-square error (RMSE) is 0.9~1.5 m s^{-1}, which

204   is smaller than the threshold of model performance criteria (2 m s^{-1}) proposed by

205   Emery et al. (2001). The positive bias in wind speed can also be reproduced in other

206   studies (Zhang et al., 2010; Gao et al., 2015; Liao et al., 2015; Qiu et al., 2017). The

207   predicted $J[NO_2]$ agrees well with the observations with R of 0.97~0.98 and NMB of

208   6.8%~6.9%. We also conduct comparisons of observed and simulated temperature

209   profiles at 08:00 and 20:00 LST in Beijing during the three episodes (Fig. S2). The

210   vertical profiles of observed temperature can be well captured by the model in these

211   three complex air pollution episodes. Generally, the WRF-Chem model can

212   reasonably reproduce the temporal variations of observed meteorological parameters.

213   **4 Results**

214   It is known that co-occurrence of $PM_{2.5}$ and O_3 pollution is frequently observed

215   nowadays over China (Dai et al., 2021). The complex air pollution characterized by

216   high $PM_{2.5}$ and O_3 levels has already received widespread attention from both

217   scientists and policy-makers. Therefore, we examine the impacts of aerosol-radiation

218   interactions on O_3 concentrations with a special focus on the complex air pollution

219   areas (CAPAs, Fig. S3) in the three episodes, where the mean simulated daily $PM_{2.5}$

220   and MDA8 (maximum daily 8-h average) O_3 concentrations are larger than 75 µg m^{-3}

221   and 80 ppb, respectively, based on the National Ambient Air Quality Standards

222   (http://www.mee.gov.cn).

223   **4.1 Impacts of aerosol-radiation interactions on meteorology**

224   Figure 4 shows the impacts of aerosol-radiation interactions on shortwave

225   radiation at the surface (BOT_SW), shortwave radiation in the atmosphere

226   (ATM_SW), PBLH, and WS_{10} during the daytime (08:00-17:00 LST) from Episode1

227   to Episode3. Analyzing the results of the interactions between aerosol and radiation

228   (the combined impacts of API and ARF), BOT_SW is decreased over the entire

229   simulated domain in the three episodes with the decreases of 93.2 W m^{-2} (20.5%),

230   100.3 W m^{-2} (19.5%) and 92.4 W m^{-2} (19.2%) over CAPAs, respectively. Contrary to

231   the changes in BOT_SW, ATM_SW is increased significantly in the three episodes

232   with the increases of 72.8 W m^{-2} (25.3%), 85.2 W m^{-2} (29.0%) and 73.7 W m^{-2} (26.4%)

233   over CAPAs, respectively. The decreased BOT_SW perturbs the near-surface energy

234   flux, which weakens convection and suppresses the development of PBL (Li et al.,

235   2017b). The mean PBLHs over CAPAs are decreased by 129.0 m (13.0%), 249.0 m

236   (20.9%) and 224.6 m (19.0%), respectively. WS_{10} exhibits overall reductions over

237   CAPAs and is calculated to decrease by 0.12 m s^{-1} (3.6%), 0.05 m s^{-1} (1.6%), and 0.12

238   m s^{-1} (3.0%) for the three episodes, respectively. We also examine the changed

239   meteorological variables caused by API and ARF respectively. As shown in Fig. S4

240   and S5, API has little impact on meteorological variables; which means the major

241   contributor to the meteorology variability is ARF.

242   **4.2 Impacts of aerosol-radiation interactions on photolysis**

243   Figure 5 shows the spatial distributions of mean daytime surface-layer $PM_{2.5}$

244 concentrations simulated by BASE cases and the changes in $J[NO_2]$ and $J[O^1D]$ due

245 to aerosol-radiation interactions from Episode1 to Episode3. When the combined

246 impacts (API and ARF) are considered, $J[NO_2]$ and $J[O^1D]$ are decreased over the

247 entire domain in the three episodes, and the spatial patterns of changed $J[NO_2]$ and

248 $J[O^1D]$ are similar to that of simulated $PM_{2.5}$. Analyzing the three simulated episodes,

249 the surface $J[NO_2]$ averaged over CAPAs are decreased by 1.8×10^{-3} s^{-1} (40.5%), 2.0

250 $\times 10^{-3}$ s^{-1} (36.8%) and 1.8×10^{-3} s^{-1} (36.0%), respectively. The decreased surface

251 $J[O^1D]$ over CAPAs are 6.1×10^{-6} s^{-1} (48.8%), 6.3×10^{-6} s^{-1} (41.4%) and 5.7×10^{-6} s^{-1}

252 (44.6%), respectively. Figure S6 exhibits the impacts of API and ARF on surface

253 $J[NO_2]$ and $J[O^1D]$. Conclusions can be summarized that $J[NO_2]$ and $J[O^1D]$ are

254 significantly modified by API and little affected by ARF.

255 **4.3 Impacts of aerosol-radiation interactions on O_3**

256 Figure 6 shows the changes in surface-layer O_3 due to API, ARF, and the

257 combined effects (denoted as ALL) from Episode1 to Episode3. As shown in Fig.

258 6(a1-a3), API alone leads to overall surface O_3 decreases over the entire domain with

259 average reductions of 8.5 ppb (10.1%), 9.0 ppb (10.6%) and 8.3 ppb (10.4%) over

260 CAPAs in the three episodes, respectively. The changes can be explained by the

261 substantially diminished UV radiation due to aerosol loading, which significantly

262 weakens the efficiency of photochemical reactions and restrains O_3 formation.

263 However, the decreased surface O_3 concentrations due to ARF are only 2.9 ppb (3.1%,

264 Fig. 6(b1)), 1.0 ppb (1.2%, Fig. 6(b2)) and 1.0 ppb (1.1%, Fig. 6(b3)) for the three

265 episodes, which indicates that API is the dominant way for O_3 reduction related to

266 aerosol-radiation interactions. Fig. 6(c1-c3) presents the combined effects of API and

267 ARF. Generally, aerosol-radiation interactions decrease the surface O_3 concentrations

268 by 11.4 ppb (13.5%), 10.0 ppb (11.9%) and 9.3 ppb (11.6%) averaged over CAPAs in

269 the three episodes, respectively.

270 **4.4 Influencing mechanism of aerosol-radiation interactions on O_3**

271 Figure 7a shows mean results of the three episodes (Episode1, Episode2 and

272 Episode3) in diurnal variations of simulated daytime surface-layer O_3 concentrations

10

from BASE, NOAPI and NOALL cases averaged over CAPAs. All the experiments (BASE, NOAPI and NOALL) present O_3 increases from 08:00 LST. It is shown that the simulated O_3 concentrations in BASE case increase more slowly than that in NOAPI and NOALL cases. To explain the underlying mechanisms of API and ARF impacts on O_3, we quantify the variations in contributions of different processes (ADV, CHEM, and VMIX) to O_3 by using the IPR analysis.

Figure 7b shows hourly surface O_3 changes induced by each physical/chemical process (i.e., ADV, CHEM, and VMIX) in BASE case averaged from Episode1 to Episode3. The significant positive contribution to the hourly variation in O_3 is contributed by VMIX, and the contribution reaches the maximum at about 09:00 LST. Since VMIX increases the surface O_3 concentrations by transporting O_3 from aloft (where O_3 concentrations are high) to the surface layer (Tang et al., 2017; Xing et al., 2017; Gao et al., 2018). The CHEM process makes negative contributions at around 09:00 and 16:00 LST, which means that the chemical consumption of O_3 is stronger than the chemical production. At noon, the net chemical contribution turns to be positive due to stronger solar UV radiation. The contribution from all the processes (NET, the sum of VMIX, CHEM, and ADV) to O_3 variation is peaked at the noon and then becomes weakened. After sunset (17:00 LST), the NET contribution turns to be negative over CAPAs, leading to O_3 decrease.

Figure 7c shows the changes in hourly process contributions caused by API averaged from Episode1 to Episode3. The chemical production of O_3 is suppressed significantly due to aerosol impacts on photolysis rates. The weakened O_3 chemical production decreases the contribution from CHEM, and results in a negative value of CHEM_DIF (-3.2 ppb h^{-1}). In contrast to CHEM_DIF, the contribution from changed VMIX (VMIX_DIF) to O_3 concentration due to API is always positive, and the mean value is +3.0 ppb h^{-1}. The positive change in VMIX due to API may be associated with the different vertical gradient of O_3 between BASE and NOAPI cases (Gao et al., 2020), as shown in Fig. 8a. The impact of API on ADV process is relatively small (-0.26 ppb h^{-1}). NET_DIF, namely the sum of VMIX_DIF, CHEM_DIF and ADV_DIF, indicates the differences in hourly O_3 changes caused by API. As shown in Fig. 7c,

11

303   NET_DIF is almost negative during the daytime over CAPAs with the mean value of -

304   0.46 ppb h^{-1}. This is because the decreases in CHEM and ADV are larger than the

305   increases in VMIX caused by API; the O$_3$ decrease is mainly attributed to the

306   significantly decreased contribution from CHEM. The maximum difference in O$_3$

307   between BASE and NOAPI appears at 11:00 LST with a value of -11.1 ppb (Fig. 7a).

308   Figure 7d shows the impacts of ARF on each physical/chemical process

309   contribution to the hourly O$_3$ variation averaged from Episode1 to Episode3. At 08:00

310   LST, the change in VMIX due to ARF is large with a value of -3.5 ppb h^{-1}, resulting in

311   a net negative variation with all processes considered. The decrease in O$_3$ reaches the

312   maximum with the value of 5.2 ppb at around 08:00 LST over CAPAs (Fig. 7a).

313   During 09:00 to 16:00 LST, the positive VMIX_DIF (mean value of +0.20 ppb h^{-1}) or

314   the positive CHEM_DIF (mean value of +0.55 ppb h^{-1}) is the major process to

315   positive NET_DIF. The positive VMIX_DIF is related to the evolution in boundary

316   layer during the daytime. The VOCs/NO$_x$ ratio is calculated to classify sensitivity

317   regimes and to indicate the possible O$_3$ responses to changes in VOCs and/or NO$_x$

318   concentrations. O$_3$ production is VOC-limited if the ratio is less than 4, and is NO$_x$-

319   limited if the ratio is larger than 15 (Edson et al., 2017; Li et al., 2017c). The ratio of

320   VOCs/NO$_x$ ranging around 4-15 indicates a transitional regime, where ozone is nearly

321   equally sensitive to both species (Sillman, 1999). As shown in Fig. S7, (a-f), O$_3$ is

322   mainly formed under the VOC-limited and the transition regimes in CAPAs. As

323   shown in Figs. S7(g-i) and S7(j-l), both the surface concentrations of VOCs and NO$_x$

324   are increased when the impacts of ARF are considered. Thus, the contribution of

325   CHEM in NOAPI is larger than that in NOALL.

326   When both impacts of API and ARF are considered, the variation pattern of the

327   difference in hourly process contribution shown in Fig. 7e is similar to that in Fig. 7c,

328   which indicates that API is the dominant factor to surface-layer O$_3$ reduction.

329   Figure 8 presents the vertical profiles of simulated daytime O$_3$ concentrations in

330   three cases (BASE, NOAPI, and NOALL), and the differences in contributions from

331   each physical/chemical process to hourly O$_3$ variations caused by API, ARF and the

332   combined effects averaged over CAPAs from Episode1 to Episode3. As shown in Fig.

8a, the O_3 concentration is lower in BASE than that in other two scenarios (NOAPI and NOALL), especially at the lower 12 levels (below 863.0 m), owing to the impacts of aerosols (API and/or ARF).

The changes in each process contribution caused by API are presented in Fig. 8b. The contribution from CHEM_DIF is -2.0 ppb h^{-1} for the first seven layers (from 27.6 to 342.8 m). Conversely, the contribution from VMIX_DIF shows a positive value under the 342.8 m (between the first layer to the seventh layer) with the mean value of +1.7 ppb h^{-1}. The positive variation in VMIX due to API may be associated with the different vertical gradient of O_3 between BASE and NOAPI again. The contributions of changed advections (ADVH_DIF and ADVZ_DIF) are relatively small, with mean values of +0.07 and -0.21 ppb h^{-1} below the first seven layers, which may result from small impact of API on wind filed (Fig. S5(a4-c4)). The net difference is a negative value (-0.44 ppb h^{-1}); API leads to O_3 reduction not only nearly surface but also aloft.

Figure 8c shows the differences in O_3 budget due to ARF. When the ARF is considered, the vertical turbulence is weakened and the development of PBL is inhibited, which makes VMIX_DIF negative at the lower seven layers (below the 342.8 m) with a mean value of -0.64 ppb h^{-1}, but the variation in CHEM caused by ARF is positive with a mean value of +0.72 ppb h^{-1}. The enhanced O_3 precursors due to ARF can promote the chemical production of O_3 (Tie et al., 2009; Gao et al., 2018). The changes of ADVZ and ADVH (ADVZ_DIF and ADVH_DIF) caused by ARF are associated with the variations in wind filed. When ARF is considered, the horizontal wind speed is decreased (Fig. ~~S7~~S8(a)), which makes ADVH_DIF positive at the lower twelve layers with a mean value of +0.25 ppb h^{-1}. However, ADVZ_DIF is negative at these layers with a mean value of -0.27 ppb h^{-1} because aerosol radiative effects decrease the transport of O_3 from the upper to lower layers (Fig. ~~S7~~S8(b)).

In Fig. 8d, the pattern and magnitude of the differences in process contributions between BASE and NOALL are similar to those caused by API, indicating the dominate contributor of API on O_3 changes. The impacts of API on O_3 both near the surface and aloft are greater than those of ARF.

Figure ~~S8~~S9 and ~~S9~~S10 detailed show the influencing mechanism of aerosol-

363 radiation interactions on O_3 in each episode. Similar variation characteristics can be
364 found among the three episodes as the mean situation discussed above, with the larger
365 impacts of API on O_3 both near the surface and aloft than those of ARF, indicating the
366 major contributor of API on O_3 reduction related with aerosol-radiation interactions.

5 Conclusions and Discussions

368 In this study, the fully coupled regional chemistry transport model WRF-Chem is
369 applied to investigate the impacts of aerosol-radiation interactions, including the
370 impacts of aerosol-photolysis interaction (API) and the impacts of aerosol-radiation
371 feedback (ARF), on O_3 during summertime complex air pollution episodes during 28
372 July to 3 August 2014 (Episode1), 8-13 July 2015 (Episode2) and 5-11 June 2016
373 (Episode3). Three sensitivity experiments are designed to quantify the respective and
374 combined impacts from API and ARF. Generally, the spatiotemporal distributions of
375 observed pollutant concentrations and meteorological parameters can be captured
376 fairly well by the model with correlation coefficients of 0.56~0.91 for pollutant
377 concentrations and 0.70~0.98 for meteorological parameters.

378 Sensitivity experiments show that aerosol-radiation interactions decrease
379 BOT_SW, WS_{10}, PBLH, $J[NO_2]$, and $J[O^1D]$ by 92.4~100.3 W m^{-2}, 0.05~0.12 m s^{-1},
380 129.0~249.0 m, 1.8×10^{-3}~2.0×10^{-3} s^{-1}, and 5.7×10^{-6}~6.3×10^{-6} s^{-1} over CAPAs,
381 and increase ATM_SW by 72.8~85.2 W m^{-2}. The changed meteorological variables
382 and weakened photochemistry reaction further reduce surface-layer O_3 concentrations
383 by up to 9.3~11.4 ppb, with API and ARF contributing 74.6%~90.0% and
384 10.0%~25.4%, respectively.

385 We further examine the influencing mechanism of aerosol-radiation interactions
386 on O_3 by using integrated process rate analysis. API can directly affect O_3 by reducing
387 the photochemistry reactions within the lower several hundred meters and therefore
388 amplify the O_3 vertical gradient, which promotes the vertical mixing of O_3. The
389 reduced photochemistry reactions of O_3 weaken the chemical contribution and reduce
390 surface O_3 concentrations, even though the enhanced vertical mixing can partly
391 counteract the reduction. ARF affects O_3 concentrations indirectly through the

changed meteorological variables, e.g., the decreased PBLH. The suppressed PBL can weaken the vertical mixing of O_3 by turbulence. Generally, the impacts of API on O_3 both near the surface and aloft are greater than those of ARF, indicating the dominant role of API on O_3 reduction related with aerosol-radiation interactions.

This study provides a detailed understanding of aerosol impacts on O_3 through aerosol-radiation interactions (including both API and ARF). The results imply that future $PM_{2.5}$ reductions will lead to O_3 increases due to weakened aerosol-radiation interactions. A recent study emphasized the need for controlling VOCs emissions to mitigate O_3 pollution (Li et al., 2019b). Therefore, tighter controls of O_3 precursors (especially VOCs emissions) are needed to counteract future O_3 increases caused by weakened aerosol-radiation interactions, and the contributions of different mitigation strategies with the impacts of aerosol-radiation interactions to O_3 air quality will be discussed detailedly in our future work.

There are some limitations to this work. The lack of secondary organic aerosol (SOA) may result in uncertainties in our model results. First, the absence of SOA would lead to underestimation of API and ARF because of the low bias in AOD, so the reductions in O_3 by API and/or ARF could have been underestimated. Second, the lack of SOA would lead to weaker heterogeneous reactions, leading to higher O_3 concentrations (Li et al., 2019c). The net effect of these two processes needs further studies. The uncertainty of the lack of secondary organic aerosols (SOA), and the missing mechanisms of some heterogeneous reactions may result in large uncertainties in the final simulation results. Gao et al. (2017) added some SOA formation mechanisms into the MOSAIC module by using the volatility basis set (VBS) in WRF-Chem and found that the surface $PM_{2.5}$ concentrations in urban Beijing were reduced by 1.9 $\mu g\ m^{-3}$ due to the weakened ARF effect during Asia-Pacific Economic Cooperation (APEC). Similar magnitude can also be found in Zhou et al. (2019) (-1.8 $\mu g\ m^{-3}$) who did not consider the impacts of SOA in WRF-Chem when analyzing the impacts of weakened ARF on $PM_{2.5}$ during APEC. Therefore, more work should be conducted to explore the impacts of ARF on $PM_{2.5}$ and O_3 concentrations under consideration of SOA in future.

Data availability

The observed hourly surface concentrations of air pollutants are derived from the China National Environmental Monitoring Center (http://www.cnemc.cn). The observed surface meteorological data are obtained from NOAA's National Climatic Data Center (https://gis.ncdc.noaa.gov/maps/ncei/cdo/hourly). The radiosonde data are provided by the University of Wyoming (http://weather.uwyo.edu/). The photolysis rates of nitrogen dioxide in Beijing are provided by Xin Li (li_xin@pku.edu.cn). The aerosol optical depth in Beijing is obtained from the AERONET level 2.0 data collection (http://aeronet.gsfc.nasa.gov/). The simulation results can be accessed by contacting Lei Chen (chenlei@nuist.edu.cn) and Hong Liao (hongliao@nuist.edu.cn).

Author contributions

HY, LC, and HL conceived the study and designed the experiments. HY and LC performed the simulations and carried out the data analysis. JZ, WW, and XL provided useful comments on the paper. HY prepared the paper with contributions from all co-authors.

Competing interests

The authors declare that they have no competing interests.

Acknowledgements

450   their support of this work.

Reference

Albrecht, B. A.: Aerosols, cloud microphysics, and fractional cloudiness, Science, 245, 1227–1230, 1989.

Chen, F. and Dudhia, J.: Coupling an Advanced Land Surface – Hydrology Model with the Penn State – NCAR MM5 Modeling System. Part I: Model Implementation and Sensitivity, Mon. Weather Rev., 129(4), 569–585, 2001.

Chen, L., Zhu, J., Liao, H., Gao, Y., Qiu, Y., Zhang, M., Liu, Z., Li, N., and Wang, Y.: Assessing the formation and evolution mechanisms of severe haze pollution in the Beijing–Tianjin–Hebei region using process analysis, Atmos. Chem. Phys., 19, 10845–10864, https://doi.org/10.5194/acp-19-10845-2019, 2019.

Dai, H., Zhu, J., Liao, H., Li, J., Liang, M., Yang, Y., and Yue, X.: Co-occurrence of ozone and $PM_{2.5}$ pollution in the Yangtze River Delta over 2013–2019: Spatiotemporal distribution and meteorological conditions, Atmos. Res., 249, 105363, 2021.

Dickerson, R. R., Kondragunta, S., Stenchikov, G., Civerolo, K. L., Doddridge, B. G., and Holben, B. N.: The impact of aerosols on solar ultraviolet radiation and photochemical smog, Science, 278, 827-830, 10.1126/science.278.5339.827, 1997.

Edson, C. T., Ivan, H.-P. and Alberto, M.: Use of combined observational- and model-derived photochemical indicators to assess the O_3-NO_x-VOC System sensitivity in urban areas, Atmosphere., 8, 22. https://doi.org/10.3390/ atmos8020022, 2017.

Emery, C., Tai, E., and Yarwood, G.: Enhanced meteorological modeling and performance evaluation for two Texas ozone episodes, in: Prepared for the Texas Natural Resource Conservation Commission, ENVIRON International Corporation, Novato, CA, USA, 2001.

Emmons, L. K., Walters, S., Hess, P. G., Lamarque, J.-F., Pfister, G. G., Fillmore, D., Granier, C., Guenther, A., Kinnison, D., Laepple, T., Orlando, J., Tie, X., Tyndall, G., Wiedinmyer, C., Baughcum, S. L., and Kloster, S.: Description and evaluation of the Model for Ozone and Related chemical Tracers, version 4 (MOZART-4), Geosci. Model Dev., 3, 43–67, doi:10.5194/gmd- 3-43-2010, 2010.

Foken, T.: 50 years of the Monin-Obukhov similarity theory, Bound.-Layer Meteor., 119, 431–437, 2006.

Gao, J., Li, Y., Zhu, B., Hu, B., Wang, L., and Bao, F.: What have we missed when studying the impact of aerosols on surface ozone via changing photolysis rates?, Atmos. Chem. Phys., 20, 10831–10844, https://doi.org/10.5194/acp-20-10831-2020, 2020.

Gao, J. H., Zhu, B., Xiao, H., Kang, H. Q., Pan, C., Wang, D. D., and Wang, H. L.: Effects of black carbon and boundary layer interaction on surface ozone in Nanjing, China, Atmos. Chem. Phys., 18, 7081–7094, https://doi.org/10.5194/acp-18-7081-2018, 2018.

Gao, M., Carmichael, G. R., Wang, Y., Saide, P. E., Yu, M., Xin, J., Liu, Z., and Wang, Z.: Modeling study of the 2010 regional haze event in the North China Plain, Atmos. Chem. Phys., 16, 1673–1691, doi:10.5194/acp-16-1673-2016, 2016a.

Gao, J., Zhu, B., Xiao, H., Kang, H., Hou, X., and Shao, P.: A case study of surface ozone source apportionment during a high concentration episode, under frequent shifting wind conditions over the Yangtze River Delta, China, Sci. Total Environ., 544, 853, https://doi.org/10.1016/j.scitotenv.2015.12.039, 2016b.

~~Gao, M., Liu, Z., Wang, Y., Lu, X., Ji, D. and Wang, L.: Distinguishing the roles of meteorology, emission control measures, regional transport, and co-benefits of reduced aerosol feedbacks in "APEC" Blue, Atmos. Environ., 167, 476 486, 420 doi:10.1016/j.atmosenv.2017.08.054, 2017.~~

Gao, Y., Zhang, M., Liu, Z., Wang, L., Wang, P., Xia, X., Tao, M., and Zhu, L.: Modeling the feedback between aerosol and meteorological variables in the atmospheric boundary layer during a severe fog–haze event over the North China Plain, Atmos. Chem. Phys., 15, 4279–4295, doi:10.5194/acp-15-4279-2015, 2015.

Goncalves, M., Jimenez-Guerrero, P., Baldasano, J.M.: Contribution of atmospheric processes affecting the dynamics of air pollution in South-Western Europe during a typical summertime photochemical episode, Atmos. Chem. Phys., 9, 849–864, doi:10.5194/acp-9-849-2009, 2009.

Grell, G. A., Peckham, S. E., Schmitz, R., Mckeen, S. A., Frost, G., Skamarock, K.,

and Eder, B.: Fully coupled "online" chemistry within the WRF model, Atmos. Environ., 39, 6957–6975, 2005.

Guenther, A., Karl, T., Harley, P., Wiedinmyer, C., Palmer, P. I., and Geron, C.: Estimates of global terrestrial isoprene emissions using MEGAN (Model of Emissions of Gases and Aerosols from Nature), Atmos. Chem. Phys., 6, 3181–3210, doi:10.5194/acp-6-3181-2006, 2006.

Hansen, J., Sato, M., and Ruedy, R.: Radiative forcing and climate response, J. Geophys. Res., 102, 6831–6864, 1997.

Haywood, J. and Boucher, O.: Estimates of the direct and indirect radiative forcing due to tropospheric aerosols: A review, Rev. Geophys., 38, 513–543, 2000.

Hong, S.-Y., Noh, Y., and Dudhia, J.: A New Vertical Diffusion Package with an Explicit Treatment of Entrainment Processes, Mon. Weather Rev., 134, 2318–2341, 2006.

Iacono, M. J., Delamere, J. S., Mlawer, E. J., Shephard, M. W., Clough, S. A., and Collins, W. D.: Radiative forcing by long-lived greenhouse gases: Calculations with the AER radiative transfer models, J. Geophys. Res., 113, D13103, doi:10.1029/2008JD009944, 2008.

Li, G., Bei, N., Tie, X., and Molina, L. T.: Aerosol effects on the photochemistry in Mexico City during MCMA-2006/MILAGRO campaign, Atmos Chem Phys, 11, 5169-5182, 10.5194/acp-11-5169-2011, 2011.

Li, J. D., Liao, H., Hu, J. L., Li, N.: Severe particulate pollution days in China during 2013-2018 and the associated typical weather patterns in Beijing-Tianjin-Hebei and the Yangtze River Delta regions, *Environmental Pollution*, 248, 74-81, 2019a.

Li, K., Jacob, D. J., Liao, H., Zhu, J., Shah, V., Shen, L., Bates, K. H., Zhang, Q., and Zhai, S.: A two-pollutant strategy for improving ozone and particulate air quality in China, Nat. Geosci., 12, 906–910, https://doi.org/10.1038/s41561-019-0464-x, 2019b.

Li, K., Jacob, D. J., Liao, H., Shen, L., Zhang, Q., and Bates, K. H.: Anthropogenic drivers of 2013–2017 trends in summer surface ozone in China, P. Natl. Acad. Sci. USA, 116, 422–427, https://doi.org/10.1073/pnas.1812168116, 2019c.

Li, M., Zhang, Q., Kurokawa, J.-I., Woo, J.-H., He, K., Lu, Z., Ohara, T., Song, Y., Streets, D. G., Carmichael, G. R., Cheng, Y., Hong, C., Huo, H., Jiang, X., Kang, S., Liu, F., Su, H., and Zheng, B.: MIX: a mosaic Asian anthropogenic emission inventory under the international collaboration framework of the MICS-Asia and HTAP, Atmos. Chem. Phys., 17, 935–963, https://doi.org/10.5194/acp-17-935-2017, 2017a.

Li, Z., Guo, J., Ding, A., Liao, H., Liu, J., Sun, Y., Wang, T., Xue, H., Zhang, H., and Zhu, B.: Aerosol and boundary-layer interactions and impact on air quality, Nat. Sci. Rev., 4, 810–833, https://doi.org/10.1093/nsr/nwx117, 2017b.

Li, K., Chen, L., Ying, F., White, S. J., Jang, C., Wu, X., Gao, X., Hong, S., Shen, J., Azzi, M. and Cen, K: Meteorological and chemical impacts on ozone formation: a case study in Hangzhou, China, Atmos. Res., 196, https://doi.org/10.1016/j.atmosres.2017.06.003, 2017c.

Liao, H., Yung, Y. L., and Seinfeld, J. H.: Effects of aerosols on tropospheric photolysis rates in clear and cloudy atmospheres, J. Geophys. Res., 104, 23697–23707, 1999.

Liao, L., Lou, S. J., Fu, Y., Chang, W. Y., and Liao, H.: Radiative forcing of aerosols and its impact on surface air temperature on the synoptic scale in eastern China [in Chinese], Chin. J. Atmos. Sci., 39, 68–82, doi: 10.3878/j.issn.1006-9895.1402.13302, 2015.

Lin, Y.-L., Farley, R. D., and Orville, H. D.: Bulk parameterization of the snow field in a cloud model, J. Clim. Appl. Meteorol., 22, 1065–1092, 1983.

Liu, Y. and Wang, T.: Worsening urban ozone pollution in China from 2013 to 2017 – Part 1: The complex and varying roles of meteorology, Atmos. Chem. Phys., 20, 6305–6321, https://doi.org/10.5194/acp-20-6305-2020, 2020.

Lo, J. C.-F., Yang, Z. L., and Pielke Sr, R. A.: Assessment of three dynamical climate downscaling methods using the Weather Research and Forecasting (WRF) model, J. Geophys. Res., 113, D09112, doi:10.1029/2007jd009216, 2008.

Lohmann, U., and Feichter, J.: Global indirect aerosol effects: A review. Atmospheric Chemistry and Physics, 5, 715–737, https://doi.org/10.5194/acp-5-715-2005, 2005.

Lou, S., Liao, H., and Zhu, B.: Impacts of aerosols on surface-layer ozone concentrations in China through heterogeneous reactions and changes in photolysis rates, Atmos. Environ., 85, 123–138, 2014.

Miao, Y., Liu, S., Guo, J., Huang, S., Yan, Y., and Lou, M.: Unraveling the relationships between boundary layer height and $PM_{2.5}$ pollution in China based on four-year radiosonde measurements, *Environmental Pollution*, https://doi.org/10.1016/j.envpol.2018.09.070, 2018.

Otte, T. L.: The impact of nudging in the meteorological model for retrospective air quality simulations. Part I: Evaluation against national observation networks. J. Appl. Meteor. Climatol., 47, 1853–1867, 2008.

Petäjä, T., Järvi, L., Kerminen, V. M., Ding, A. J., Sun, J. N., Nie, W., Kujansuu, J., Virkkula, A., Yang, X., Fu, C. B., Zilitinkevich, S., and Kulmala, M.: Enhanced air pollution via aerosol-boundary layer feedback in China, Sci. Rep., 6, 18998, doi:10.1038/srep18998, 2016.

Qiu, Y., Liao, H., Zhang, R., and Hu, J.: Simulated impacts of direct radiative effects of scattering and absorbing aerosols on surface layer aerosol concentrations in China during a heavily polluted event in February 2014, J. Geophys. Res. Atmos., 122, 5955–5975, doi:10.1002/2016JD026309, 2017.

Sillman, S.: The relation between ozone, NO_x and hydrocarbons in urban and polluted rural environments, Atmos. Environ., 33, 1821-1845, https://doi.org/10.1016/S1352-2310(98)00345-8, 1999.

Skamarock, W., Klemp, J. B., Dudhia, J., Gill, D. O., Barker, D. M., Duda, M., Huang, X. Y., Wang,W., and Powers, J. G.: A description of the advanced research WRF version 3, NCAR technical note NCAR/TN/u2013475, 2008.

Tang, G. Q., Zhu, X.W., Xin, J. Y., Hu, B., Song, T., Sun, Y., Zhang, J. Q., Wang, L. L., Cheng, M. T., Chao, N., Kong, L. B., Li, X., and Wang, Y. S.: Modelling study of boundary-layer ozone over northern China – Part I: Ozone budget in summer, Atmos. Res., 187, 128–137, 2017.

Tie, X., Geng, F., Li, P., Gao, W., and Zhao, C.: Measurement and modelling of ozone variability in Shanghai, China, Atmos. Environ., 43, 4289–4302, 2009.

Wang, W., Li, X., Shao, M., Hu, M., Zeng, L., Wu, Y., and Tan, T.: The impact of aerosols on photolysis frequencies and ozone production in Beijing during the 4-year period 2012–2015, Atmos. Chem. Phys., 19, 9413–9429, https://doi.org/10.5194/acp19-9413-2019, 2019.

Wild, O., Zhu, X., and Prather, M. J.: Fast-J: Accurate simulation of in- and below-cloud photolysis in tropospheric chemical models, J. Atmos. Chem., 37, 245–282, doi:10.1023/A:1006415919030, 2000.

Wu, J., Bei, N., Hu, B., Liu, S., Wang, Y., Shen, Z., Li, X., Liu, L., Wang, R., Liu, Z., Cao, J., Tie, X., Molina, L. T., Li, G.: Aerosol-photolysis interaction reduces particulate matter during wintertime haze events, Proc. Natl. Acad. Sci. USA, 117, 9755–9761, 2020.

Xing, J., Wang, J. D., Mathur, R., Wang, S. X., Sarwar, G., Pleim, J., Hogrefe, C., Zhang, Y. Q., Jiang, J. K., Wong, D. and Hao, J. M.: Impacts of aerosol direct effects on tropospheric ozone through changes in atmospheric dynamics and photolysis rates, Atmos. Chem. Phys., 17, 9869–9883, https://doi.org/10.5194/acp-17-9869-2017, 2017.

Zaveri, R. A. and Peters, L. K.: A new lumped structure photochemical mechanism for large-scale applications, J. Geophys. Res., 104, D23, 30387–30415, https://doi.org/10.1029/1999JD900876, 1999.

Zaveri, R. A., Easter, R. C., Fast, J. D., and Peters, L. K.: Model for simulating aerosol interactions and chemistry (MOSAIC), J. Geophys. Res., 113, D13204, https://doi.org/10.1029/2007JD008782, 2008.

Zhang, X., Zhang, Q., Hong, C. P., Zheng, Y. X., Geng, G. N., Tong, D., Zhang, Y. X., and Zhang, X. Y.: Enhancement of $PM_{2.5}$ concentrations by aerosol-meteorology interactions over China. Journal of Geophysical Research: Atmospheres,123, 1179–1194, https://doi.org/10.1002/2017JD027524, 2018.

Zhang, Y., Wen, X.-Y., and Jang, C. J.: Simulating chemistry– aerosol–cloud–radiation–climate feedbacks over the continental US using the online-coupled Weather Research Forecasting Model with chemistry (WRF/Chem), Atmos. Environ., 44, 3568–3582, doi:10.1016/j.atmosenv.2010.05.056, 2010.

630　Zhao, H.; Zheng, Y., and Li, C. Spatiotemporal distribution of PM$_{2.5}$ and O$_3$ and their
631　　interaction during the summer and winter seasons in Beijing, China. Sustainability,
632　　10, 4519, 2018.

633　Zhou, M., Zhang, L., Chen, D., Gu, Y., Fu, T. M., Gao, M., Zhao, Y., Lu, X. and Zhao,
634　　B.: The impact of aerosol-radiation interactions on the effectiveness of emission
635　　control measures, Environmental Research Letters, 14(2), 024002,
636　　https://doi.org/10.1088/1748-9326/aaf27d, 2019.

637　Zhu, J., Chen, L., Liao, H., and Dang, R.: Correlations between PM$_{2.5}$ and Ozone over
638　　China and Associated Underlying Reasons, Atmosphere, 352, 1–15,
639　　https://doi.org/10.3390/atmos10070352, 2019.

640　Zhu, J., Chen, L., Liao, H., Yang, H., Yang, Y., and Yue, X.: Enhanced PM$_{2.5}$
641　　Decreases and O$_3$ Increases in China During COVID-19 Lockdown by Aerosol-
642　　Radiation Feedback, Geophys. Res. Lett., 48,
643　　https://doi.org/10.1029/2020GL090260, 2021.

1 **Table 1.** Physical parameterization options used in the simulation.

Options	Schemes
Microphysics scheme	Lin (Purdue) scheme (Lin et al.,1983)
Cumulus scheme	Grell 3D ensemble scheme
Boundary layer scheme	Yonsei University PBL scheme (Hong et al., 2006)
Surface layer scheme	Monin-Obukhov surface scheme (Foken, 2006)
Land-surface scheme	Unified Noah land-surface model (Chen and Dudhia, 2001)
Longwave radiation scheme	RRTMG (Iacono et al., 2008)
Shortwave radiation scheme	RRTMG (Iacono et al., 2008)

2
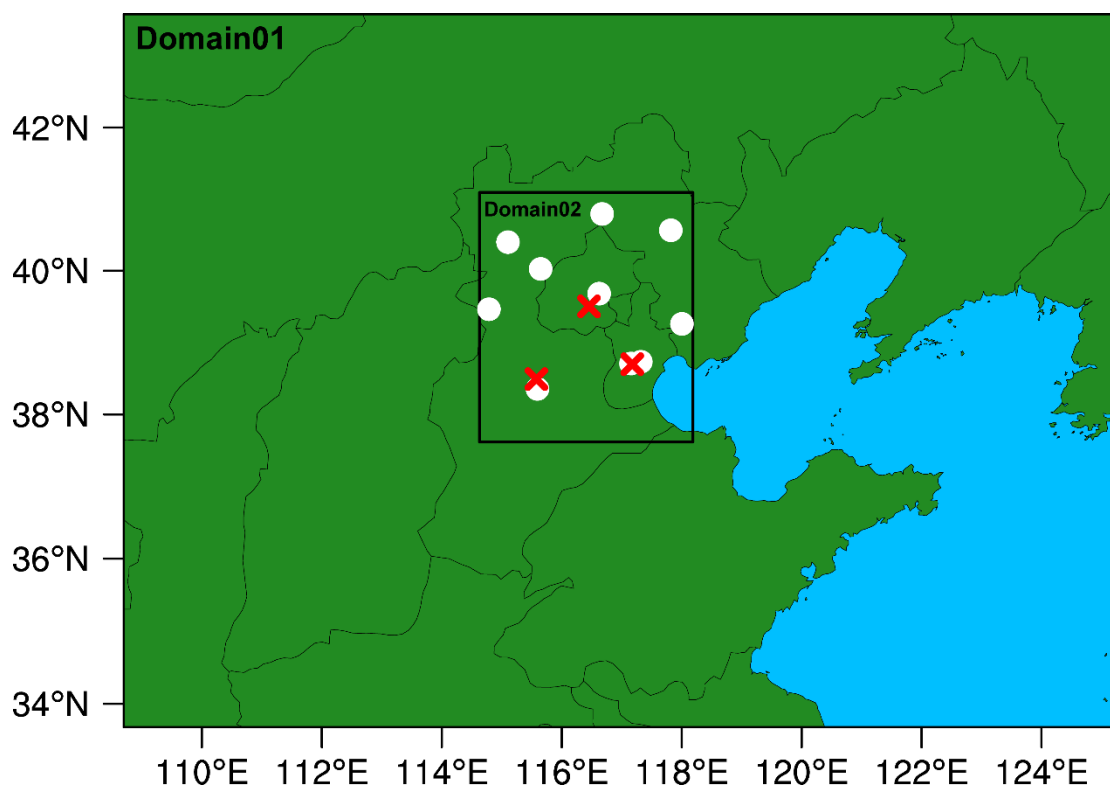
Figure 1. Map of the two WRF-Chem modeling domains with the locations of meteorological (white dots) and environmental (red crosses) observation sites used for model evaluation.
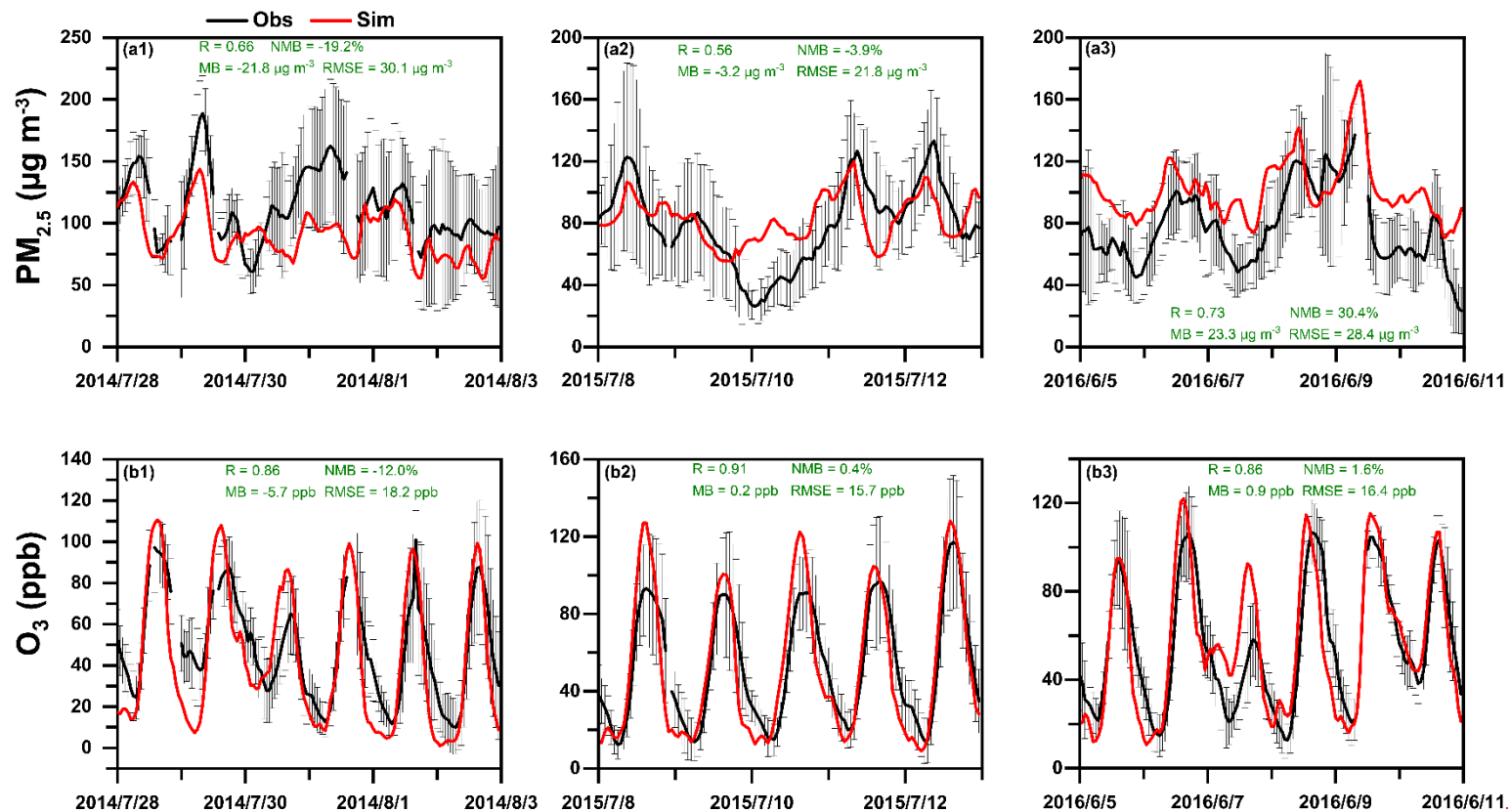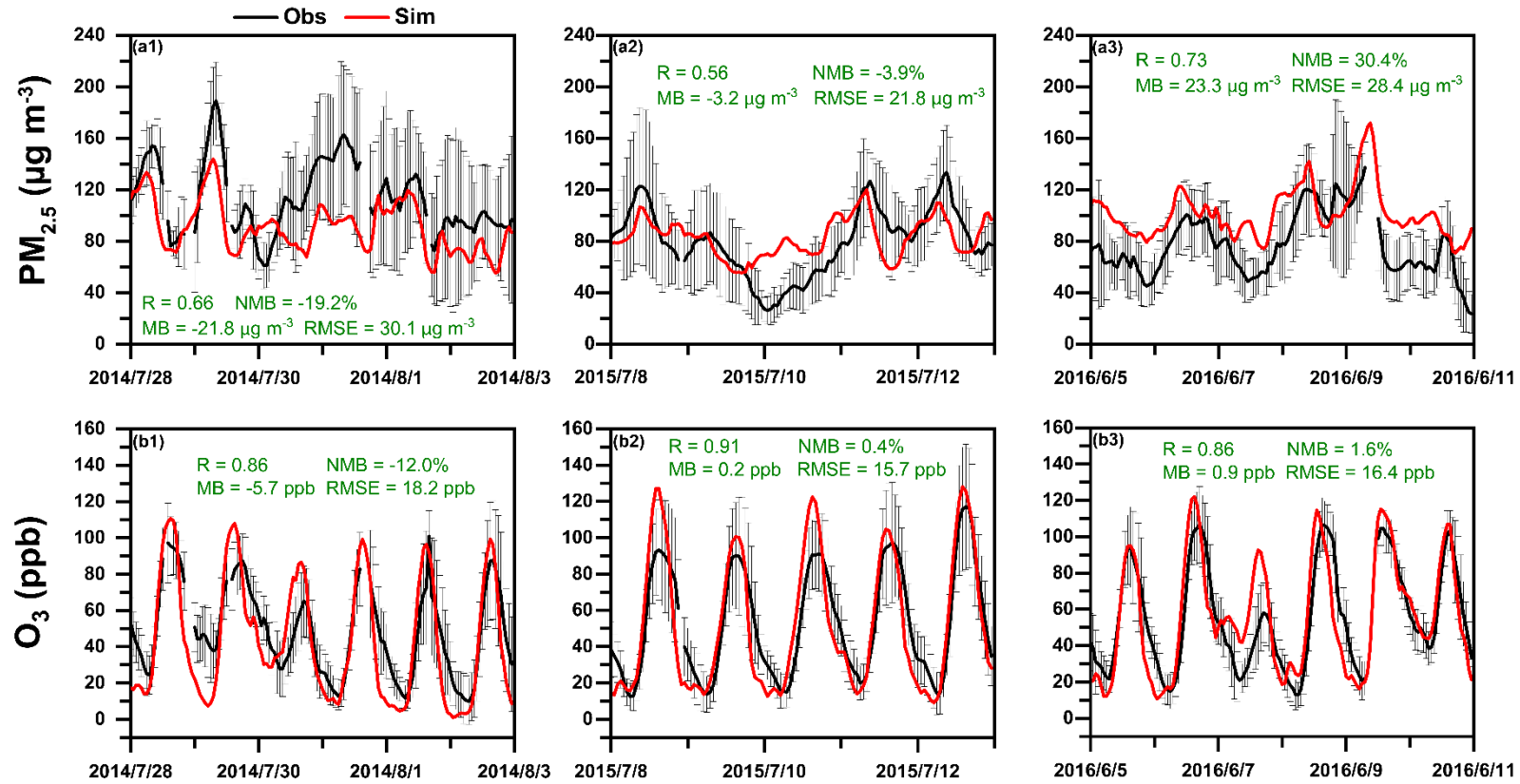
Figure 2. Time series of observed (black) and simulated (red) hourly surface (a) PM$_{2.5}$ and (b) O$_3$ concentrations averaged over the thirty-two observation sites in Beijing, Tianjin, and Baoding during 28 July to 3 August 2014 (Episode1, a1-b1), 8-13 July 2015 (Episode2, a2-b2) and 5-11 June 2016 (Episode3, a3-b3). The error bars represent the standard deviations. The calculated correlation coefficient (R), mean bias (MB), normalized mean bias (NMB) and root-mean-square error (RMSE) are also shown.
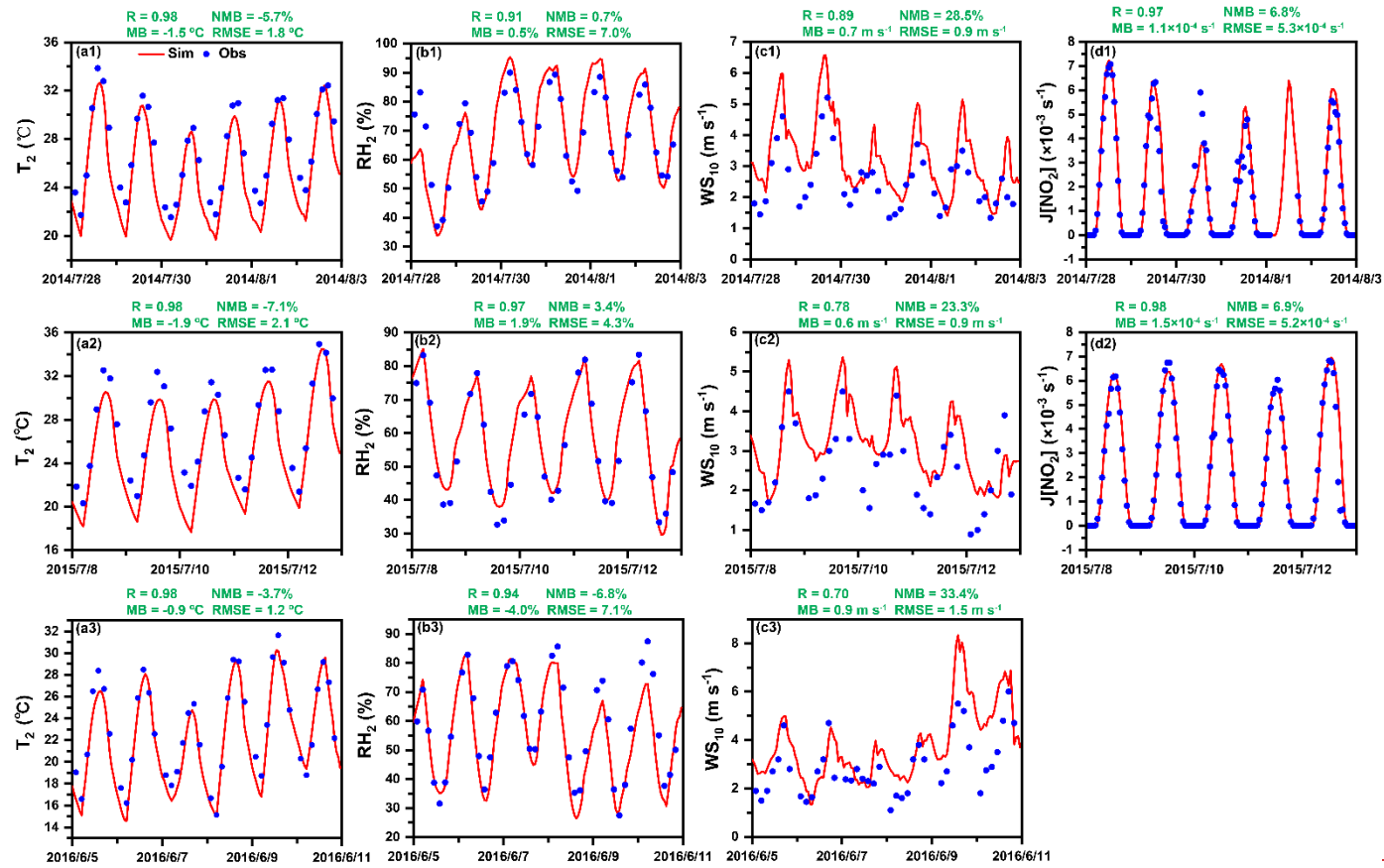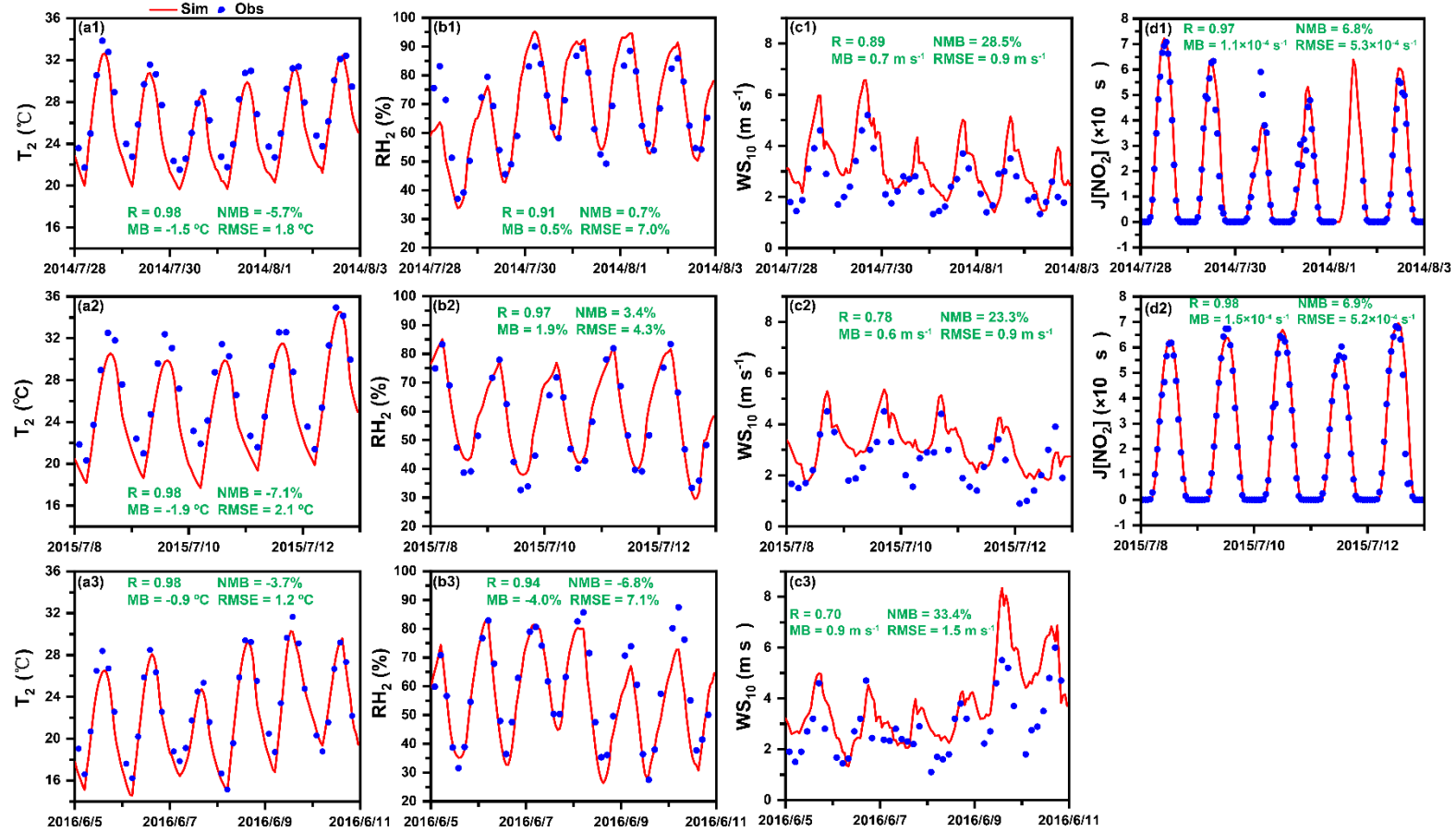
**Figure 3.** Time series of 3-hourly observed (blue dots) and hourly simulated (red lines) (a) 2-m temperature (T_2), (b) 2-m relative humidity (RH_2), (c) wind speed at 10 m (WS_{10}) averaged over ten meteorological observation stations, and (d) surface photolysis rate of NO_2 ($J[NO_2]$) during 28 July to 3 August 2014 (Episode1, a1-d1), 8-13 July 2015 (Episode2, a2-d2) and 5-11 June 2016 (Episode3, a3-c3). The calculated correlation coefficient (R), mean bias (MB), normalized mean bias (NMB) and root-mean-square error (RMSE) are also shown.
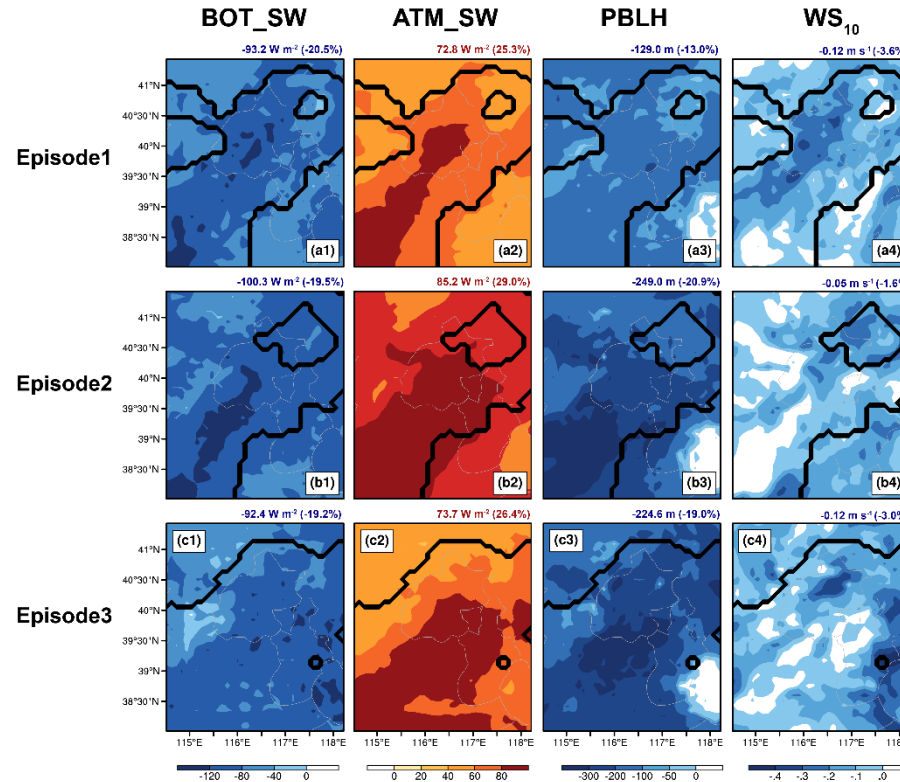
Figure 4. The impacts of aerosol-radiation interactions on shortwave radiation at the surface (BOT_SW), shortwave radiation in the atmosphere (ATM_SW), PBL height (PBLH), and 10-m wind speed (WS_{10}) in the daytime (08:00-17:00 LST) during 28 July to 3 August 2014 (Episode1), 8-13 July 2015 (Episode2) and 5-11 June 2016 (Episode3). The regions sandwiched between two black lines are defined as the complex air pollution areas (CAPAs) where the mean daily $PM_{2.5}$ and MDA8 O_3 concentrations in BASE case are larger than 75 µg m^{-3} and 80 ppb. The calculated changes (percentage changes) averaged over CAPAs are also shown at the top of each panel.
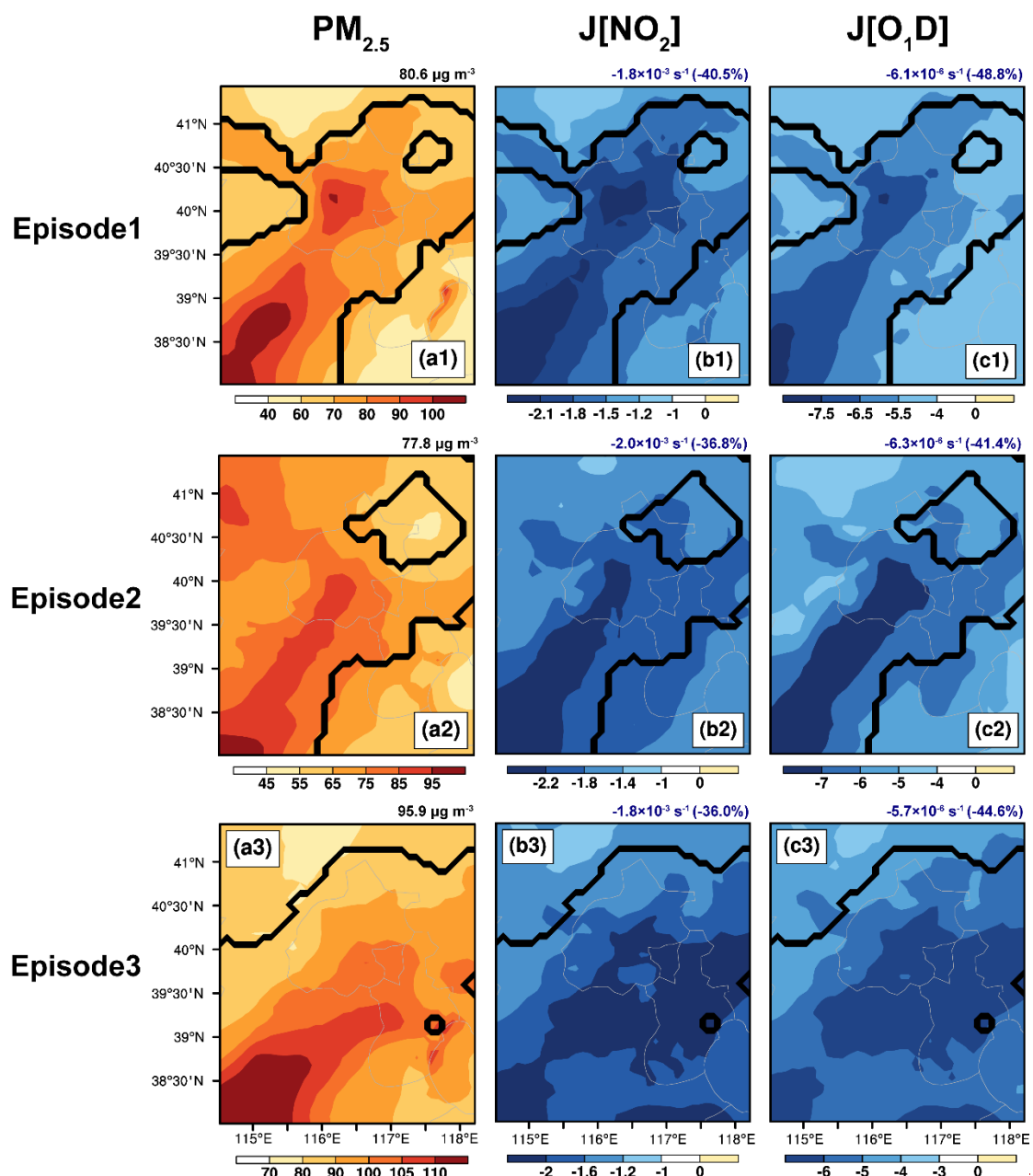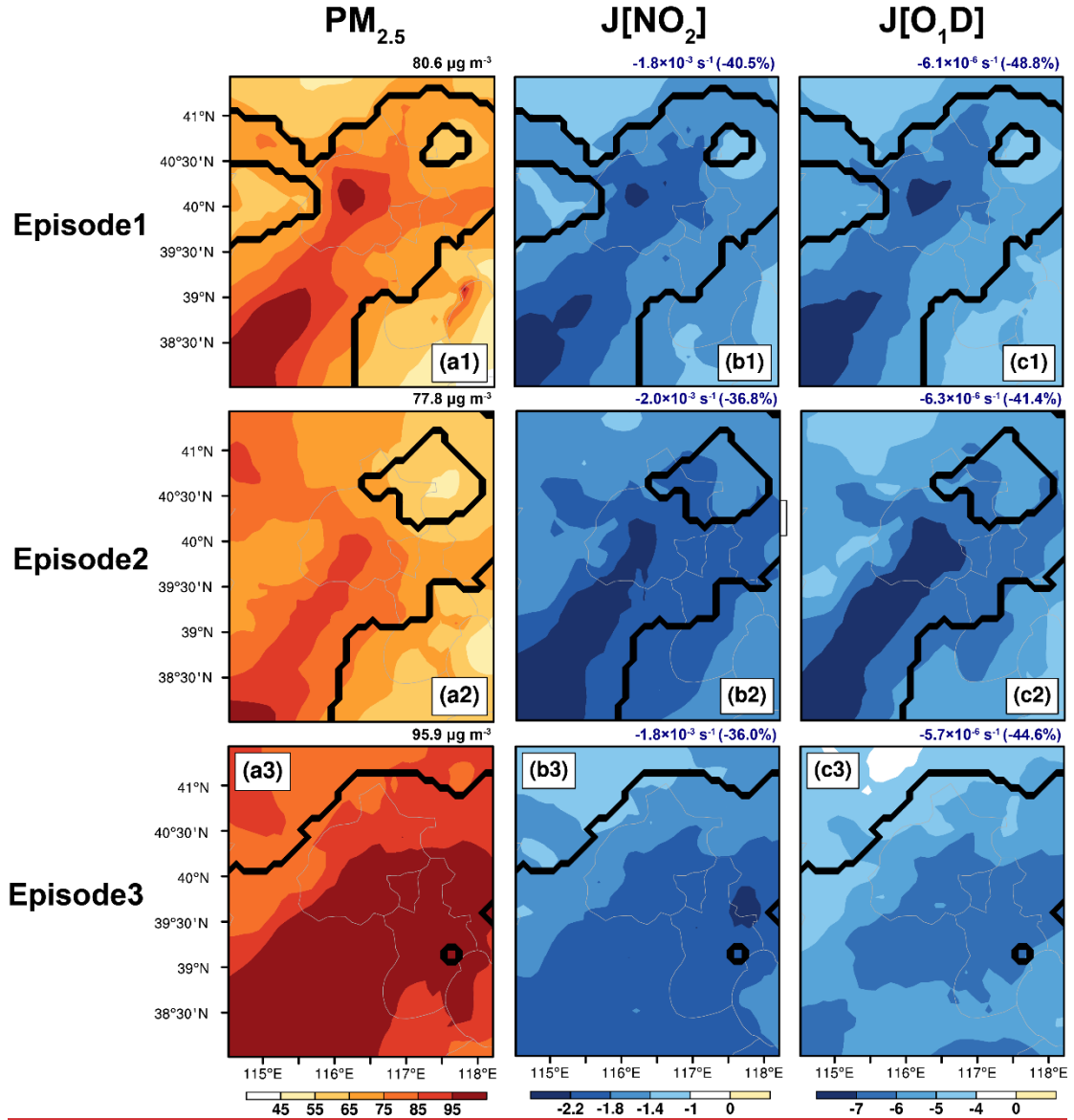
Figure 5. Spatial distributions of (a) simulated surface-layer $PM_{2.5}$ concentrations in BASE cases, and the changes in surface (b) $J[NO_2]$ and (c) $J[O^1D]$ due to aerosol-radiation interactions in the daytime (08:00-17:00 LST) during 28 July to 3 August 2014 (Episode1), 8-13 July 2015 (Episode2) and 5-11 June 2016 (Episode3). The calculated values (percentage changes) avaraged over CAPAs are also shown at the top of each panel.
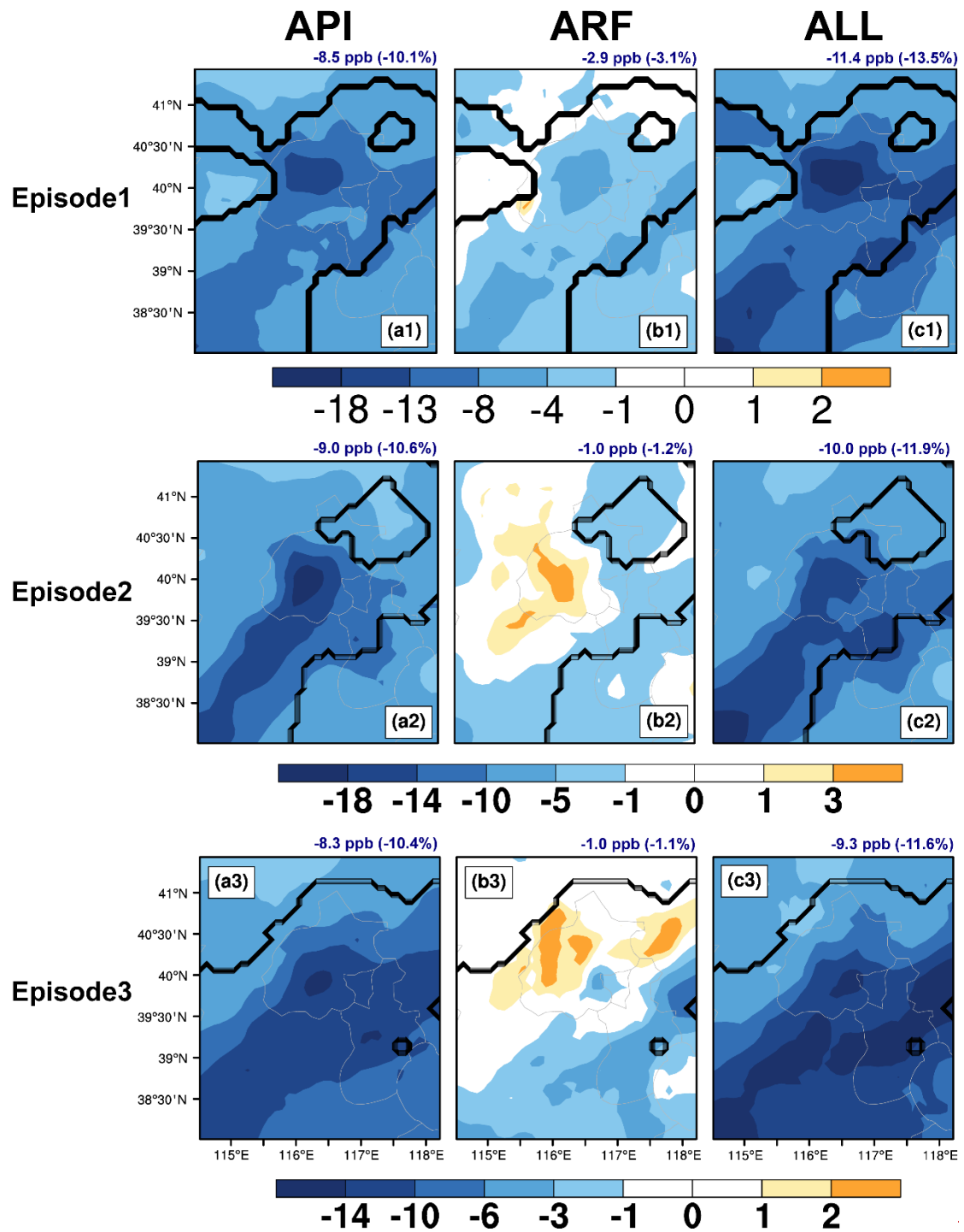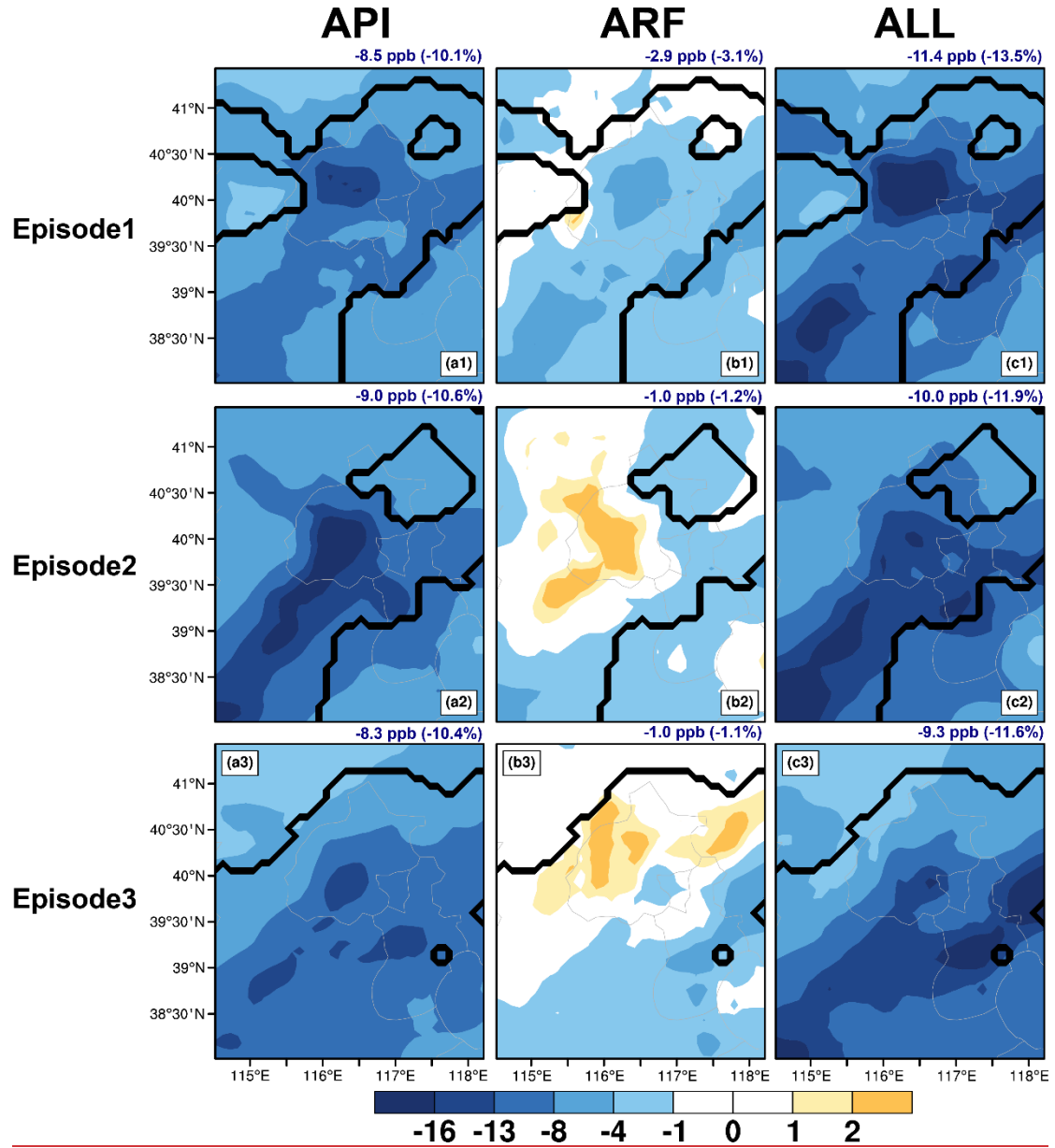
Figure 6. The changes in surface-layer ozone due to (a) aerosol-photolysis interaction (API), (b) aerosol-radiation feedback (ARF), and (c) the combined effects (ALL, defined as API+ARF) in the daytime (08:00-17:00 LST) during 28 July to 3 August 2014 (Episode1), 8-13 July 2015 (Episode2) and 5-11 June 2016 (Episode3). The calculated mean changes (percentage changes) avaraged over CAPAs are also shown at the top of each panel.

1

2
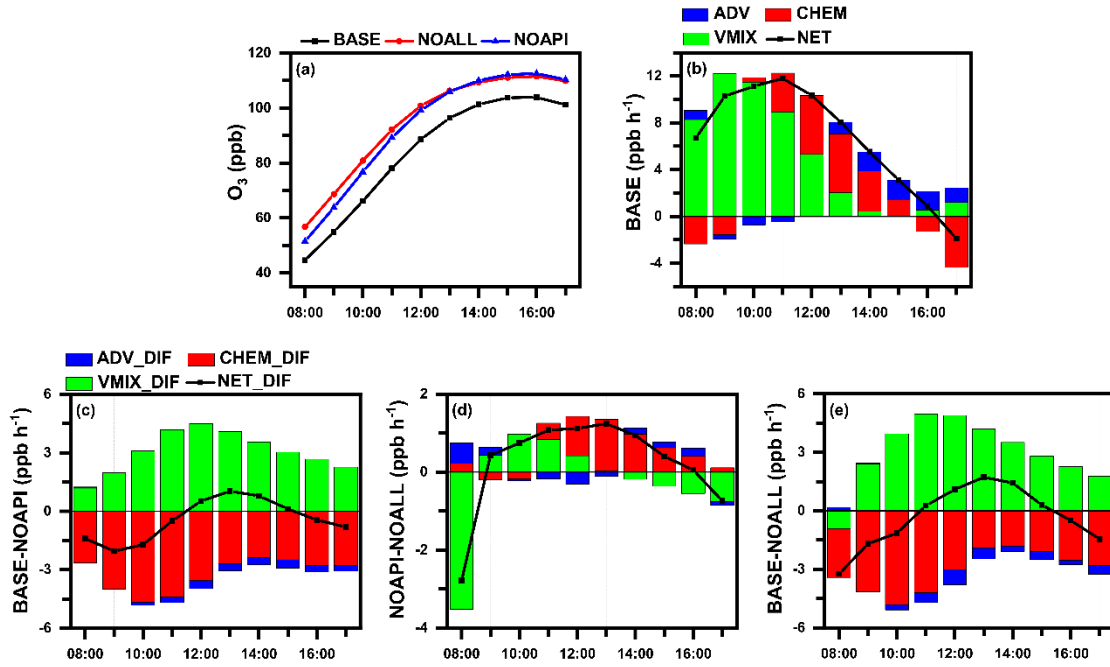
Figure 7. Temporal evolution characteristics of aerosol-radiation interactions on O_3
averaged over the three episodes. (a) Diurnal variations of simulated surface O_3
concentrations in BASE (black dotted line), NOAPI (blue dotted line), and NOALL
(red dotted line) cases over CAPAs. (b) The hourly surface O_3 changes induced by
each physical/chemical process using the IPR analysis method in BASE case. (c-e)
Changes in hourly surface O_3 process contributions caused by API (BASE minus
NOAPI), ARF (NOAPI minus NOALL), and ALL (BASE minus NOALL) over
CAPAs during the daytime (08:00-17:00 LST). The black lines with squares denote
the net contribution of all processes (NET, defined as VMIX+CHEM+ADV).
Differences of each process contribution are denoted as VMIX_DIF, CHEM_DIF,
ADV_DIF, and NET_DIF.

14

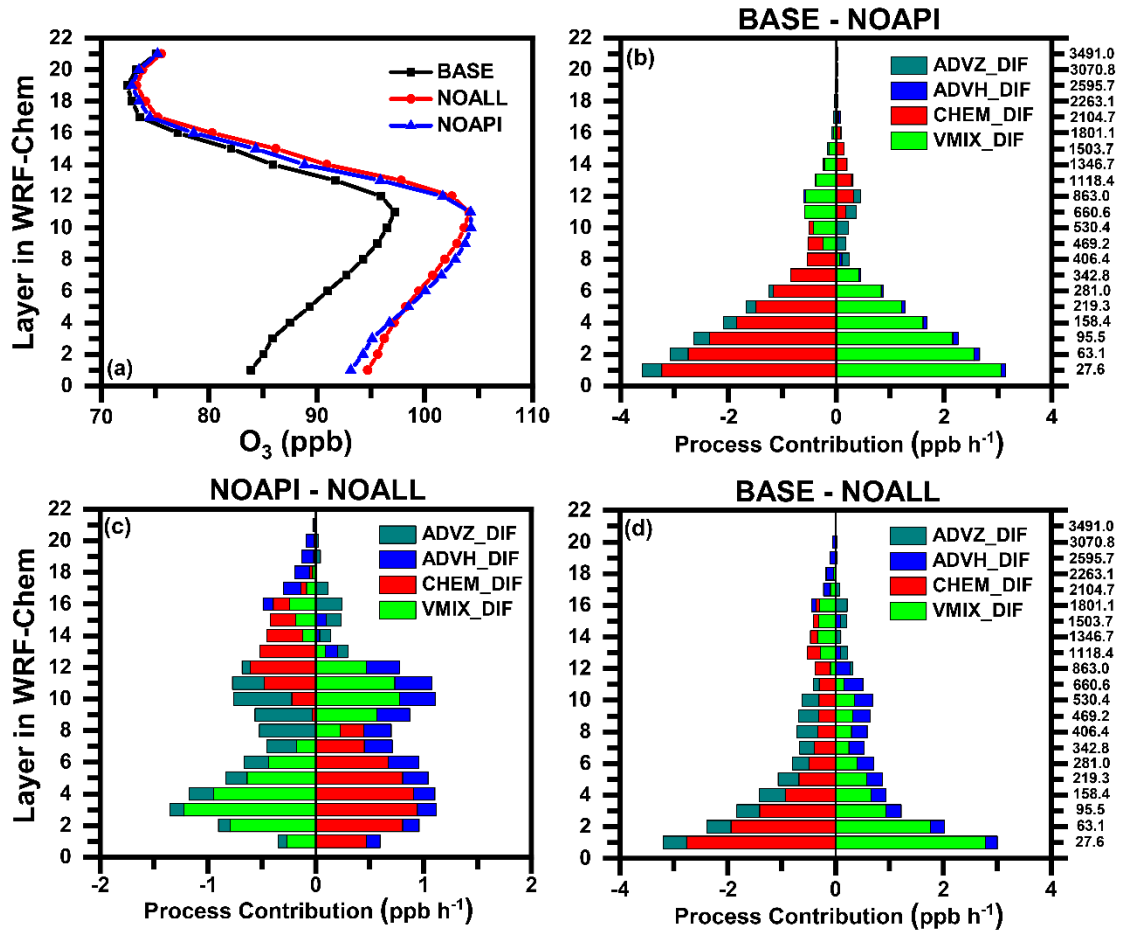**Figure 8.** The impacts of aerosol-radiation interactions on vertical O_3 averaged over the three episodes. (a) Vertical profiles of simulated O_3 concentrations in BASE (black dotted line), NOAPI (blue dotted line), and NOALL (red dotted line) cases over CAPAs. (b-d) Changes in O_3 budget due to API, ARF, and ALL over CAPAs during the daytime (08:00-17:00 LST). Differences of each process contribution are denoted by ADVZ_DIF, ADVH_DIF, CHEM_DIF, and VMIX_DIF.